Robust Brain Tumor Diagnosis in Clinical MRI Scenarios: A Non-Negative Matrix Tri-Factorization Approach for Missing Modality Imputation

MEHMOOD, Waqas <http://orcid.org/0000-0002-5432-3863>, SAJJAD, Aqsa <http://orcid.org/0009-0004-0082-8788>, AKMAL, Muhammad <http://orcid.org/0000-0002-3498-4146> and KAINAT, Fatima <http://orcid.org/0000-0002-5412-1989>

IEEE Access
Multidisciplinary | Rapid Review | Open Access Journal

Received 22 July 2025, accepted 15 August 2025, date of publication 22 August 2025, date of current version 8 September 2025.

Digital Object Identifier 10.1109/ACCESS.2025.3601623

RESEARCH ARTICLE

Robust Brain Tumor Diagnosis in Clinical MRI Scenarios: A Non-Negative Matrix Tri-Factorization Approach for Missing Modality Imputation

WAQAS MEHMOOD[1], (Member, IEEE), AQSA SAJJAD[1], MUHAMMAD AKMAL[2], AND FATIMA KAINAT[3]

[1]Shaukat Khanum Memorial Cancer Hospital and Research Centre, Lahore 54000, Pakistan
[2]Department of Electrical Engineering, National University of Computer and Emerging Sciences, Lahore 54000, Pakistan
[3]Chaudhry Muhammad Akram Teaching and Research Hospital, Lahore 54000, Pakistan

Corresponding author: Waqas Mehmood (waqasbme@gmail.com)

ABSTRACT Brain tumors are among the most common and aggressive diseases, often resulting in significantly reduced life expectancy at advanced stages. Consequently, effective treatment planning becomes crucial for improving patient quality of life. However, in real-world clinical settings, MRI data often suffer from missing modalities i.e., certain MRI sequences (such as T1, T2, or FLAIR) are unavailable due to patient movement, time constraints, or equipment failure. This partial data availability leads to reduced performance of deep learning-based diagnostic systems, which typically rely on input. To address this gap, we propose a novel framework based on Non-negative Matrix Tri-Factorization (NMTF) that reconstructs missing portions of MRI data and enables reliable classification even when input is incomplete. Unlike previous studies that either ignore missing data or assume fixed missing patterns, our model adaptively factorizes available information into three low-rank non-negative matrices, enabling the recovery of missing features. To evaluate the effectiveness of proposed framework, six deep neural network classifiers are initially trained and tested on complete MRI scans (both 2D and 3D). Subsequently, varying amounts of data (from 10% to 50%) from sagittal slice are deliberately removed, and the classifiers are re-applied, resulting in a noticeable drop in performance due to the missing information. To address this, the proposed NMTF method is used to reconstruct the missing portions of the MRI data. The classifiers are then re-evaluated on the NMTF-recovered scans. This approach is validated across two distinct datasets. Results indicate that the average classification accuracy improves by approximately 10% $\pm$ 2 when comparing performance on incomplete MRI scans versus those reconstructed via NMTF.

INDEX TERMS Brain tumor, deep learning, MRI scans, non-negative matrix tri-factorization.

I. INTRODUCTION

Brain tumor classification is an essential procedure in medical evaluation in computer-assisted diagnostics (CAD). Time-consuming and complex identification of brain tumors from the results of Magnetic Resonance Imaging (MRI) inspection results in wrong detection and classification. Such a complexity is due to the fact that brain tumor segmentation is based on a series of complex steps and modules. MRI has continued to be the leading method of diagnosis of brain tumor because it is capable of producing detailed images, which differentiates soft normal and abnormal brain tissues. Notwithstanding its relevance, medical practitioners are exposed to immense difficulties when it comes to timely and accurate diagnosis of gliomas. The developments in the deep learning have enabled medical image analysis and diagnostics in the process of automation, which increase the accuracy and of brain tumor segmentation [1].

The associate editor coordinating the review of this manuscript and approving it for publication was Prakasam Periasamy.

Manual brain tumor classification on MRI scans presents significant challenges, demanding extensive effort, being susceptible to human error, and yielding inconsistent outcomes across different radiologists. Driven by the need for enhanced accuracy and consistency in identifying brain tumors, automated segmentation techniques have seen considerable advancements. The automated brain tumor segmentation process has experienced major progress because of deep learning algorithms, which include Convolutional Neural Networks (CNNs), U-Net and V-Net. The superior performance of these models over traditional methods stems from their advantages in achieving high accuracy, consistent outcomes, and robust reproducibility. These medical systems utilize MRI analysis algorithms for automated tumor segmentation, which not only alleviates radiologist workload but also enhances the reliability of healthcare results [2]. Automated systems demonstrate significant utility in clinical workflows due to their capacity for processing extensive data collections and their ability to iteratively enhance performance through continuous data assimilation [3]. The proficiency of automated systems in handling substantial data volumes and their iterative performance enhancement via continuous data assimilation render them highly applicable to clinical workflows [4]. Enhanced performance in brain tumor detection is achieved through deep learning techniques, primarily leveraging ResNet and DenseNet architectures' exceptional ability to process complex data. These advancements mitigate the computational constraints inherent in earlier models, thereby offering improved flexibility for the detection of diverse tumor pathologies, imaging modalities, and patient populations [5].

The current need for precise brain tumor diagnosis grows stronger as brain cancer cases continue to escalate. Each year in the United States the medical community diagnoses about 23,000 new brain cancer cases primarily because gliomas represent the most common and fastest-growing brain tumor type [6]. Healthcare professionals need to detect gliomas early and precisely segment tumors because this enables successful treatment planning. Modern medical practices rely on accurate tumor segmentation for constructing simulated 3D surgical resection models as well as for designing specific radiotherapy and chemotherapy treatments [7]. Comprehensive assessment of tumor progression and evaluation of treatment efficacy necessitate the consistent application of MRI scans across both the diagnostic and therapeutic phases. Automated segmentation methodologies facilitate the acquisition of raw data for continuous treatment follow-ups, owing to their high precision in identifying even minute alterations in tumor morphology [8]. Technical methods minimize the human errors that appear, when experts perform manual segmentation work by producing consistent outcomes [9].

The progression of medical imaging has facilitated the incremental integration of deep learning segmentation models into contemporary healthcare delivery. These advanced models exhibit substantial potential to yield enhanced diagnostic accuracy, optimized therapeutic regimens, and minimized adverse effects, collectively contributing to superior patient outcomes. Concurrently, these algorithms demonstrate considerable scalability across diverse clinical environments, offering tangible benefits to both medical personnel and their respective patient cohorts [10].

The current trajectory of personalized medicine is substantially bolstered by these advancements. Precise automated tumor segmentation facilitates enhanced surgical planning and optimized radiotherapy and chemotherapy protocols by ensuring the preservation of healthy brain tissue during complete tumor resection. Concurrently, the economic viability of the healthcare sector is improved through these advanced technologies, as they mitigate manual labor and expedite diagnostic processes, rendering them particularly advantageous for deployment in resource-constrained environments. Ultimately, automated segmentation yields considerable economic benefits by concurrently optimizing clinical workflows and augmenting healthcare accessibility [11].

The reconstruction of missing features in MRI data within this study leverages the inherent low-rank structure and non-negativity of medical imaging data. MRI scans, particularly those of the brain, exhibit strong spatial and contextual correlations, meaning neighboring pixels and slices often contain redundant or related information. This redundancy allows us to approximate the original high-dimensional data using a lower-dimensional representation without significant loss of detail. By exploiting this physical property, NMTF techniques decompose the data into interpretable basis components and encoding coefficients under the constraint of non-negativity, which aligns naturally with the physical property of MRI intensities being non-negative by nature. This structured decomposition allows the missing values to be estimated based on observed data patterns, resulting in a realistic and consistent recovery that preserves the structural integrity of brain tissues.

The novelty of this study lies in the following key contributions:

a) This is the first work to apply a NMTF matrix factorization-based method for recovering missing parts of sagittal slices in brain MRI scans used for tumor diagnosis.

b) We conduct a comparative analysis between matrix and tensor factorization techniques for missing data (MD) recovery, demonstrating the superior performance of the tensor-based approach.

c) To evaluate the effect of data recovery on deep learning classifiers, we initially trained and tested the models on complete MRI datasets, achieving a mean accuracy of 89%. Subsequently, we introduced varying levels of missing data (10% to 50%), which led to a noticeable drop in performance-accuracy decreased to 82% for 10% missing data and to 70% for 50%. After applying the proposed recovery methods, classifier accuracy improved to 86% and 80% for 10% and 50% missing data, respectively. These results highlight the effectiveness of the recovery framework in mitigating the adverse impact of missing data.

II. LITERATURE REVIEW

The field of medical image analysis has witnessed rapid progress with the integration of deep learning techniques [28], [29], particularly in addressing challenges such as incomplete data and robust image reconstruction. Several studies have explored missing data imputation in MRI using approaches like statistical interpolation, nearest neighbor, and patch-based filling, but these often fail to preserve spatial and contextual integrity. More recent research has adopted generative models (e.g., GANs, VAEs) to reconstruct missing or corrupted regions in medical images with improved fidelity. However, many of these methods either rely heavily on supervised learning with large paired datasets or are not scalable. Our work builds upon these foundations by proposing a matrix factorization-based approach that is scalable and handles missing feature-level data and then systematically evaluate the impact of data recovery on deep learning classifiers and compare NMTF with other matrix and tensor factorization techniques to validate the advantages of higher-order modeling.

In the study [12], authors introduced a curated real-world multi-modal dataset MMIST-CCRCC that includes MRI modality as well. In that dataset, they further provided benchmarks for up to 90% missing data for MRI. The missing data is recovered by encoder-decoder approach. Encoder first replaced the missing modality vector by zeros, whereas decoder reconstructs that missing modality. However, they have not shown the effect of recovering missing data on accuracy of DL-classifiers. In another study [13], Deep Learning Generative Adversarial Network (DLGAN) is proposed to regenerate the MRI images. It showed enhanced image reconstruction performance along with addressing vanishing-gradient problem as well. However, DLGAN is based on deep learning model, which is complex and requires huge time for training and computational resources. The authors in [14] employed a dual-objective adversarial learning framework to recover up to 50% missing sagittal slices from MRI scans. The task at hand was to predict progression from mild cognitive impairment (MCI) to Alzheimer's disease (AD) in presence of missing data. In [15], authors presented a work in which they first removed the noise by employing Altered Phases Preserving Dynamic Range Compression (APPDRC), then they employed Golden Eagle Optimization (GEO)-optimized GAN to further reduce noise from MRI scans. However, the presence of missing data is not explored with much detail in the work. In another study [16], CNN with various ML algorithms is employed in presence of missing data. However, the missing data was replaced simply by applying median based on neighboring values. As MRI images have fine structural details (e.g., tumor boundaries, tissue textures) therefore technique like Median filtering blurs or distorts important edges, which are critical for diagnosis or automated classification. In the study [17], the authors proposed to recover missing data simply by replacing the highest occurrence value. Such strategy can create unrealistic patches and be misleading. Moreover, it is unable to utilize inter-modal correlations or temporal consistency in 3D scans. Recently, transformers have also been employed to recover missing data. For example, in the study [18], authors employed Multi-Modal Mixing Transformer (3MT) for classification of MRI scans in presence of noise. However, the authors reported the issue of scalability and quadratic increase of computational complexity when the number of pixels increase.

III. METHODOLOGY

Our proposed framework involves four key stages: preprocessing, data matrix construction, feature extraction, and classification. First, we apply six deep neural networks-based classifiers on complete MRI scans (both 2D and 3D). Next, Fig. 1 shows that we deliberately remove data from 10% to 50%, and again employ classifiers. As expected, performance of classifiers is reduced because of missing data. Finally, we apply proposed NMTF to recover missing data as shown in Fig. 2, which completes the scans. And classifiers are now employed on NMTF-recovered MRI Scans.

A. DETAILS OF DATASETS

1) DATASET 1

The dataset employed in this research originates from the BraTS 2020 Challenge data, a component of the Medical Segmentation Decathlon (MSD) contest [26]. It consists of 750 fully labeled 3D MRI images, each presented as standardized NIfTI (.nii.gz) files. Every scan within the dataset measures 240 × 240×155 voxels, and includes four MRI modalities: T1, T1c, T2, and FLAIR. Crucially, each study is accompanied by its ground truth tumor segmentation map.

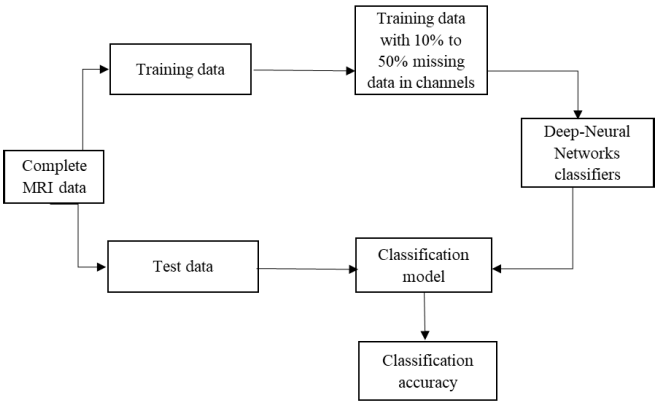

FIGURE 1. Classification by using the incomplete MRI scans.

2) DATASET 2

For this study, we also utilized the Brain Tumor Image Dataset from Kaggle [27], created by pkdarabi. This dataset comprises 3064 MRI brain images, each 640 × 640 pixels, and including corresponding tumor masks.

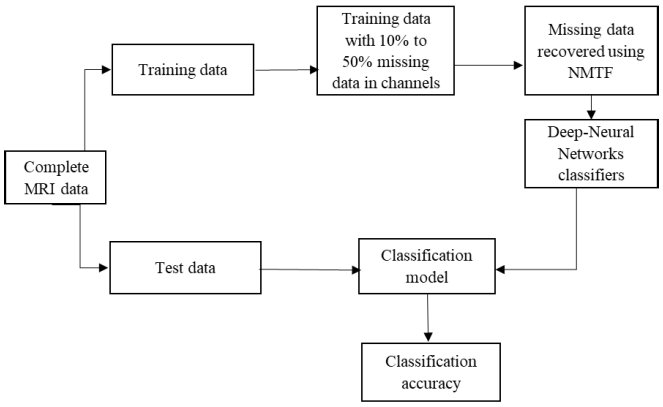

FIGURE 2. Classification by using the NMTF-recovered MRI scans.

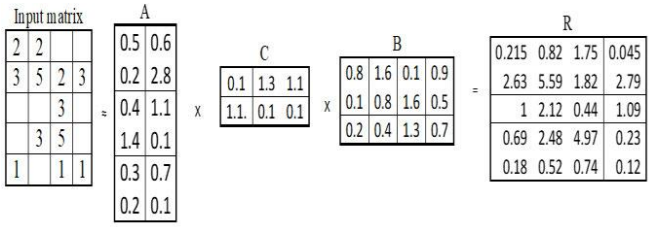

FIGURE 3. Decomposition and reconstruction of input matrix in presence of missing data.

B. PREPROCESSING

Preprocessing helps make the raw medical imaging data ready for effective and successful deep learning analysis. The Dataset 1 includes 3D MRI scans in the NIfTI format (.nii.gz), containing scans from brain tumor patients with their expert-made segmentation labels. The dataset was accessed from Google Drive, and processed using Google Colab in this study. The study used 450 3D MRI volumes, with 360 selected for training, and 90 for testing how well the model performs. The MRI images and the related labels had their size limited to $32 \times 32 \times 16$ voxels so less processing time would be needed. The changes enabled important features to remain intact during training with limited memory usage. Each volume was adjusted to fit in a range from 0 to 1 by dividing each voxel by the maximum intensity. Dataset 2 holds 2D images for a similar application, had its images all sized to 256×256 pixels. Because the data is standardized, deep learning models that require precise-sized input can be used.

C. FEATURE EXTRACTION

Feature extraction is a crucial process in machine learning and data analysis, where raw data is transformed into a set of informative characteristics or ''features'' between healthy and tumor groups. The goal is to reduce the dimensionality of the data, while retaining its most important aspects, making it easier for algorithms to detect patterns, and make accurate predictions.

1) NON-NEGATIVE MATRIX TRI-FACTORIZATION (NMTF)

NMTF focuses on decomposing a non-negative data into meaningful lower-dimensional representations $U \in \mathbb{R}_+^{p\times q}$ by multiplying three matrices A, B and C together, where $A \in \mathbb{R}_+^{p\times r_1}$, $B \in \mathbb{R}_+^{r_1\times r_2}$, and $C \in \mathbb{R}_+^{p\times r_2}$ [19] as shown in Fig. 3. NMTF reduces the size of input data U, removes noise from it, and explains the underlying structure of the data [20]. In comparison to traditional non-negative matrix factorization, NMTF decomposes the input matrix into three factor matrices instead of two. The latent matrix A creates a space of r_1 dimensions that tries to resemble U's rows. Correspondingly, C explains a column-space made up from r_1, r_2 vectors, and B specifies the way the two separate latent spaces interact. This reconstruction error between the two matrices U and $\hat{Y} = AB^TC^T$ is measured by the Frobenius distance D_{FRO} as given in eq. 1:

$$D_{FRO}\left(U \left\| AB^TC^T\right.\right) = \left\| U - \left\| AB^TC^T \right\|_{FRO}^2 \quad (1)$$

Moreover, different loss functions such as the Kullback-Leibler divergence, Alpha divergence [21], and Beta divergence [22] could be used for optimization. In fact, we can use other variants of D_{FRO} by adding further regularization terms to its loss function. In clustering applications, we may require orthogonality between A and C so that their latent vectors reflect the transfer of row and column objects to different clusters. In this case, including the A^TA regularization term in the loss function will ensure the latent vectors in A are no longer parallel. The latent matrices can be made sparse by using $\|A\|_1$ *and* $\|C\|_1$ regularization in the loss function [23].

2) MULTIPLICATIVE UPDATE RULES FOR NMTF

Generally, NMTF has a non-convex objective function, yet fixing all but one latent matrix makes it convex [19]. To reach a stationary point, the objective function is minimized for each of A, B and C. Initially, the latent matrices are initialized with random values, and then iteratively updated using gradient-based steps until convergence is achieved. Convergence is typically assessed by monitoring changes in the objective function (as defined in Eq. 1) over successive iterations. Following this, we provide a concise overview of the current multiplicative update rules. Applying the Karush-Kuhn-Tucker condition means $\frac{\partial L}{\partial A_{ij}} = 0$ to find the partial derivative of A at the i-th row and j-th column, and update the matrix accordingly. The final rule for updating A is shown below:

$$A \leftarrow A \odot \left(UCB^T\right) \oslash \left(ABC^T CB^T\right) \quad (2)$$

Here, the $\odot$ stands for Hadamard product, and the $\oslash$ represents Hadamard division. This rule can also be found among the update rules in the process.

$$C \leftarrow C \odot U^TAB \oslash CB^TA^TAB \quad (3)$$

To obtain the update rule for latent matrix B, we differentiate the objective function with respect to B, and use the

Karush-Kuhn-Tucker conditions. As a result, a new update rule for B is found by this procedure given as:

$$B \leftarrow B \odot \left(A^T UC\right) \oslash \left(A^T ABC^T C\right) \tag{4}$$

NMTF can also be solved using alternating least squares (ALS). In ALS, the method iterates, and each loop requires a least-squares solver applied to the latent matrix [24]. We derive the objective in Eq. 1 for the different latent matrices, and enforce positivity on them using a simple rule. Using this procedure, we get the following rules for updating the system:

$$A \leftarrow \left[\left(UCB^T \left(BC^T CB^T\right)^{-1}\right)\right]_+ \tag{5}$$

$$C \leftarrow \left[\left(U^T AB\right)\left(B^T A^T AB\right)^{-1}\right)\right]_+ \tag{6}$$

$$B \leftarrow \left[\left(A^T A\right)^{-1} \left(A^T UC\right)\left(C^T C\right)^{-1}\right]_+ \tag{7}$$

where $[\cdot]_+$ is the projection to the non-negative space, calculated as $A_{ij} = 0$ if $A_{ij} < 0$ else A_{ij}. The ALS approach is equivalent to the second-order quasi-Newton approach [25].

3) PROJECTED GRADIENTS FOR NMTF

Gradient descent optimizes matrix factorization by incrementally adjusting parameters along the gradient's descent direction. The learning rate (step size) presents a trade-off: excessively large values risk divergence, while overly small values reduce convergence speed.

The projected gradient method addresses constrained optimization in NMTF by iteratively updating latent factors while enforcing non-negativity through projection. It selects an optimal learning rate to maximize progress along the gradient direction without violating the constraints. Notably, with a step size of 1, it reduces to multiplicative updates, while maintaining stricter non-negativity guarantees than ALS.

For NMTF, we obtain the following rule to update the latent matrix U:

$$\begin{aligned} P_A &= A - A \oslash ((ABC^T CB^T) \odot (UCB^T)) \\ \eta_A &= \frac{\sum \left(P_A \odot \left(\left(ABC^T CB^T\right) - \left(UCB^T\right)\right)\right)}{Tr\left(\left(\left(BC^T C\right)\left(BP_A^T P_A\right)\right)\right)} \\ A &\leftarrow [A - \eta_A P_A]_+ \end{aligned} \tag{8}$$

The matrix P_A is the projection matrix, and η_A represents how large a step to take. The method to update the latent matrix C is given as:

$$\begin{aligned} P_C &= C - C \oslash \left(\left(CB^T A^T AB\right) \odot \left(U^T AB\right)\right) \\ \eta_C &= \frac{\sum \left(P_C \odot \left(\left(CB^T A^T AB - U^T AB\right)\right)\right)}{T_r\left(\left(BP_C^T P_C\right)\left(B^T A^T A\right)\right)} \\ C &\leftarrow [C - \eta_C P_C]_+ \end{aligned} \tag{9}$$

Here, P_C is the projection matrix, and η_C is used as the step size when the algorithm runs. The update rule for latent matrix $\mathbf{B}$ is as follows:

$$\begin{aligned} P_B &= B - B \oslash \left(\left(A^T ABC^T C\right) \odot \left(A^T UC\right)\right) \\ \eta_b &= \frac{\sum \left(P_B \odot \left(A^T \mathrm{ABC}^T \mathrm{C} - A^T UC\right)\right)}{T_r\left(\left(A^T AP_B\right)\left(C^T CP_B^T\right)\right)} \\ B &\leftarrow [B - \eta_b P_B]_+ \end{aligned} \tag{10}$$

Here, P_B is the projection matrix, and η_B is used as the step size when the algorithm runs.

4) COORDINATE DESCENT FOR NMTF

Many machine learning techniques such as support vector machines and non-negative matrix factorization (NMF), use coordinate descent. It has been reported that coordinate descent provides new advantages for NMF compared to other approaches such as in two-factor NMF and multiplicative updates. Instead of moving the latent matrices together as in multiplicative and gradient-based methods, the coordinate descent approach independently calculates the gradient of each vector in each matrix.

It is a first-order method, just like multiplicative update rules, alternating least squares and projected gradients. Rather than computing the derivatives of the full latent matrix, coordinate descent handles scalars or vectors in the matrix, and reuses part of its earlier results immediately. Updates to the first vector in the latent matrix are fed into the second one, and the first two vectors are combined in computing the third. Because you can order the updates differently, coordinate descent is available in three versions: cyclic, stochastic and greedy. Updates follow the same order in each cycle with a cyclic method, whereas a stochastic algorithm update choices randomly. A greedy method updates the vector that results in the greatest improvement to the objective function.

In the following section, we present the method to update the parameters using cyclic coordinate descent in the NMTF:

$$a_{.i} \longleftarrow a_{.i} + \left[\frac{\left(\left(UCB^T\right)_{.i} - \left(ABC^T CB^T\right)_{.i}\right)}{b_i C^T Cb_{i.}^T}\right]_+ \tag{11}$$

$$c_{.j} \longleftarrow c_{.j} + \left[\frac{\left(\left(U^T AB\right)_{.j} - \left(CB^T A^T AB\right)_{.j}\right)}{b_j C^T Cb_{j.}^T}\right]_+ \tag{12}$$

$$b_{ij} \longleftarrow b_{ij} + \left[\frac{\left(\left(A^T UC\right)_{ij} - \left(A^T ABC^T C\right)_{ij}\right)}{a_{i.}^T a_{.i} c_{.j}^T c_{.j}}\right]_+ \tag{13}$$

Here, $a_{.i}$ represents the i-th column of A, and $c_{.j}$ represents the j-th row of C. Update rules for A and C are successively applied to every column in A and C, where b_{ij} update is applied to each element in latent matrix B.

D. CLASSIFICATION

To assess the performance of the proposed framework, following deep neural networks–based classifiers were used: U-Net, V-Net, DenseNet, ResNet, CNN and FCN. The details of the parameters for each of the model are given in Table 1 to

show the training procedure. CNN is a fundamental type of neural network specifically designed to process data with a known grid-like topology, such as images (2D grid of pixels). On the other hand, FCN is a type of CNN architecture specifically designed for semantic segmentation, where the goal is to classify each pixel in an image. FCNs replace the traditional fully connected layers with convolutional layers. This allows the network to output a spatial map (a segmentation mask) rather than a single vector. ResNet is used for classification of images. However, it introduces residual connections to address the problem of vanishing gradient. U-Net is a specific type of Fully Convolutional Network (FCN), which combines encoder-decoder architecture with skip connections between corresponding resolution levels in the encoder and decoder paths. V-Net is an extension of the U-Net architecture specifically designed for 3D volumetric medical image segmentation. It maintains the core principles of U-Net but adapts them for 3D data (e.g., CT scans, MRI sequences that are inherently 3D). It uses 3D convolutions (instead of 2D convolutions) in both the encoder and decoder paths.

Experiments were conducted using a Core i5-13450HX CPU, NVIDIA GeForce RTX 3050 GPU, 8 GB RAM, and a 256 GB SSD. The dataset was split 70:30 into training and validation sets using the segmented ROI masks as labels. A 10-fold cross-validation was used to reduce the bias.

1) U-NET

Due to GPU memory limitations, the normalized 3D MRI brain scans (original size: 240 × 240×155) were resampled to 128 × 128×1 by extracting only the middle slice.

A U-Net architecture with 23 convolutional layers was employed in study as shown in Fig. 4. It consists of an encoder-decoder structure: the encoder compresses spatial information using repeated 3 × 3 convolutions, ReLU activations, and 2 × 2 max-pooling layers, while the decoder reconstructs the segmentation map via 2 × 2 transposed convolutions and concatenation with encoder features (skip connections).

The final 1 × 1 convolution maps feature vectors to two classes (ROI and background), producing a segmented output. A sigmoid activation function is used for binary classification. The fully convolutional design (no dense layers) allows variable input sizes. Skip connections aid feature reuse and help address vanishing gradients by maintaining continuous gradient flow. For image-level classification, global average pooling is applied to the bottleneck features, followed by fully connected layers and a softmax function.

2) V-NET

V-Net, originally designed for prostate segmentation from MRI, uses an encoder-decoder structure shown in Fig. 5. The encoder compresses the input via down-sampling, while the decoder restores the original resolution using deconvolutions. Both sides contain four resolution blocks, each with one to three convolutional units. Residual connections within blocks and skip connections between encoder and decoder help improve segmentation accuracy. Each block starts and ends with a 1×1 × 1.3D convolution to reduce parameters and memory usage. For image-level classification, features from the bottleneck (e.g., 256 channels of 6 × 6×6) are passed through Global Average Pooling to obtain a compact vector, then fed into dense layers. A softmax layer produces the final classpredictions.

3) DENSENET

The DenseNet model employed in this study follows an encoder-decoder architecture as shown in Fig. 6. To accelerate training and improve performance, a pre-trained DenseNet121 is used as the encoder. The input image passes through a series of dense blocks in the encoder, which extract rich feature representations. These features are then passed to the decoder, whose role is to progressively upsample and reshape the features. Skip connections are used to transfer semantic information from corresponding encoder layers to the decoder, helping retain spatial details. The decoder includes 3 × 3 convolution layers with batch normalization and ReLU activations. The final layer of the decoder applies a 1 × 1 convolution followed by a sigmoid activation. As illustrated in Fig. 6, the architecture combines DenseNet's powerful feature extraction with UNet's spatial reconstruction capabilities. Although some information is lost during downsampling via max-pooling, skip connections help restore it, enabling precise localization especially for preserving tumor boundaries. The decoder concludes by producing high-dimensional features that are fed into a softmax layer for classification.

4) RESNET

The ResNet model shown in Fig. 7 begins with an initial convolutional layer that uses 64 filters of size 7 × 7 with a stride of 2. This is followed by batch normalization and a ReLU activation function to maintain consistency across the feature maps. A 2 × 2 max pooling layer is then applied to reduce the spatial dimensions and extract dominant features.

Next, the model enters the first residual stage, which consists of one convolutional block and two identity blocks. Each of these blocks utilizes filter sets of [64, 64, 256] with a stride of 1, allowing the network to learn and retain fine-grained details from the input.

In the third stage, the architecture includes another convolutional block and three identity blocks, using filters [128, 128, 512] and a stride of 2. This stage deepens the network and captures more abstract representations. The fourth stage is more extensive, containing one convolutional block and five identity blocks, each using filters [256, 256, 1024] with 3×3 convolution sizes and a stride of 2. This further enhances feature extraction at a deeper level.

The fifth stage comprises one convolutional block and two identity blocks, each using filters [512, 512, 2048] with a stride of 2, enabling the model to learn high-level, complex patterns. Finally, the network concludes with a fully connected layer that maps the extracted features to the num-

TABLE 1. Details of the parameters for employed models.

Model	Optimizer	Learning Rate	Loss Function	Epochs
U-Net	Adam	1e-4	Binary Cross-Entropy (BCE)	100
V-Net	Adam	1e-4	Dice Loss	100
DenseNet	Adam	1e-3	Categorical Cross-Entropy (Softmax)	60
ResNet	Stochastic Gradient Descent (Momentum=0.9)	1e-3	Categorical Cross-Entropy	100
CNN	Adam	1e-3	Cross-Entropy	50
FCN	Adam	1e-4	Cross-Entropy	100

ber of output classes using a softmax activation. The output is then flattened to produce the final classification result.

5) CNN

The architecture shown in Fig. 8 illustrates a 3D Convolutional Neural Network (CNN) designed for image-level classification of 3D medical data, such as MRI scans for tumor detection. The architecture begins with an encoder-like feature extraction backbone, where multiple 3D Convolutional Layers (followed by ReLU activations) progressively learn hierarchical patterns from the input images. These convolutional layers are interspersed with 3D Max Pooling layers, which reduce the spatial dimensions of the feature maps, thereby compressing the data and making the learned features more robust to minor variations in the input. This downsampling process allows the network to capture increasingly abstract and high-level representations of the entire 3D volume, effectively acting as a powerful feature extractor.

Next, the architecture incorporates a dedicated classification head, which starts with a Global Pooling (GP) Layer, which is crucial for image-level tasks. This layer aggregates the 3D feature maps from the deepest part of the convolutional backbone into a single 1D feature vector by averaging or taking the maximum across all spatial dimensions. This flattened representation is then fed into a Fully Connected (FC) Layer, which learns to map these high-level features to the final classification output. For a multi-class classification problem, the final output layer used a softmax activation function to produce a probability score, indicating the likelihood of the input image belonging to one of the different classes.

IV. RESULTS

Given that the main question of this study is related to the effect of using information of images with a tensor analysis approach in improving the classification results of patients with brain tumor and healthy individuals, it is necessary to compare the process with the conventional approach, and without considering the concepts of tensor analysis, and finally compare them. Therefore, in the following section, first classifiers are trained and tested on original images (with no missing data), which is a conventional approach. Afterwards, missing data from 10% to 50% is introduced deliberately, and classifiers are trained and tested on them. Lastly, missing data is recovered by various approaches, and classifiers are trained and tested on them.

A. PERFORMANCE OF PROPOSED STRATEGY ON DATASET 1

The performance of the proposed framework is assessed on Dataset 1 in terms of its ability to recover the underlying factors. Table 2 shows the performance of NMF, CP-WOPT and NMTF for different percentages of missing data. It is evident that NMTF outperformed other methods as it achieved minimum RME even in the worst case, when 50% of the data was missing. Table 2 demonstrates that even if a significant percentage, e.g., 50%, of the tensor entries are missing, the NMTF factor matrices can still be recovered successfully.

The ROC curves for DenseNet, when employed on Dataset 1 and Dataset 2 are shown in Fig. 9 and Fig. 10, respectively. The Fig. 9(a) and Fig. 10(a) show accuracy trends for both training and testing datasets. It can be observed that the training accuracy increases steadily, reaching approximately 90%, while the testing accuracy stabilizes around 82%. The Fig. 9(b) and Fig. 10(b) presents the Root Mean Error (RME) over the same epochs. The training error drops rapidly and flattens below 0.1, while the testing error decreases more gradually and stabilizes around 0.2.

As reference accuracies are required for comparison, hence Table 3 presents the accuracies of six classifiers, when they are trained on data with no missing values (complete dataset). Table 3 shows that U-Net and V-Net achieved an accuracy of 92.2%. However, DenseNet achieved the accuracy of up to 96%, outperforming all other methods. The state-of-the-art CNN achieved an accuracy of 81.11%. As we have obtained the reference accuracies, next we employed six classifiers on the incomplete Dataset 1. The results are reported in Fig. 11. For the case of 10% missing data, DenseNet outperformed other classifiers by achieving 90% accuracy. However, other classifiers could not achieve such accuracy. The same is true for other percentages of missing data. Furthermore, it must be noted that as percentage of missing data increase, accuracies deteriorate significantly.

Fig. 13 shows the classification accuracy of various deep learning models (Unet, Vnet, Densenet, Resnet, CNN, and FCN) for Dataset 1 with three imputation methods: NMTF, CP-WOPT, and NMF. The first section (left-most part) of the

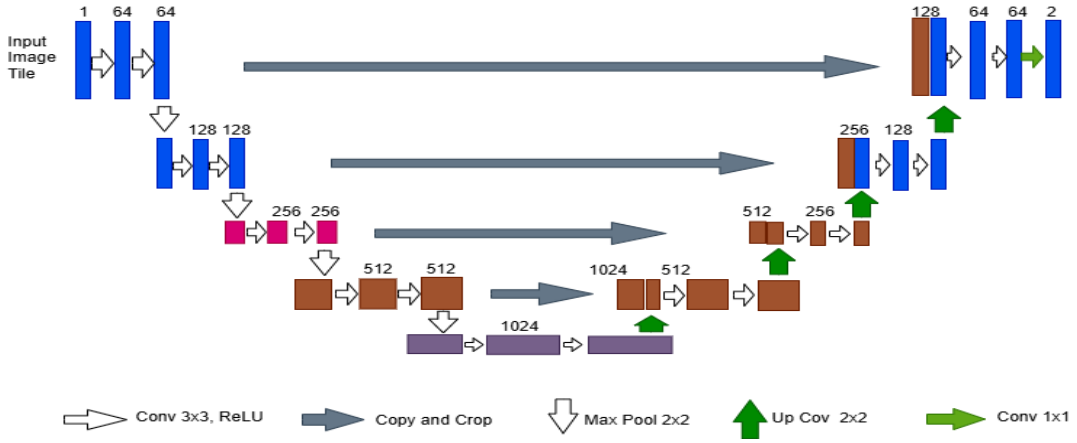

FIGURE 4. Architecture of U-Net.

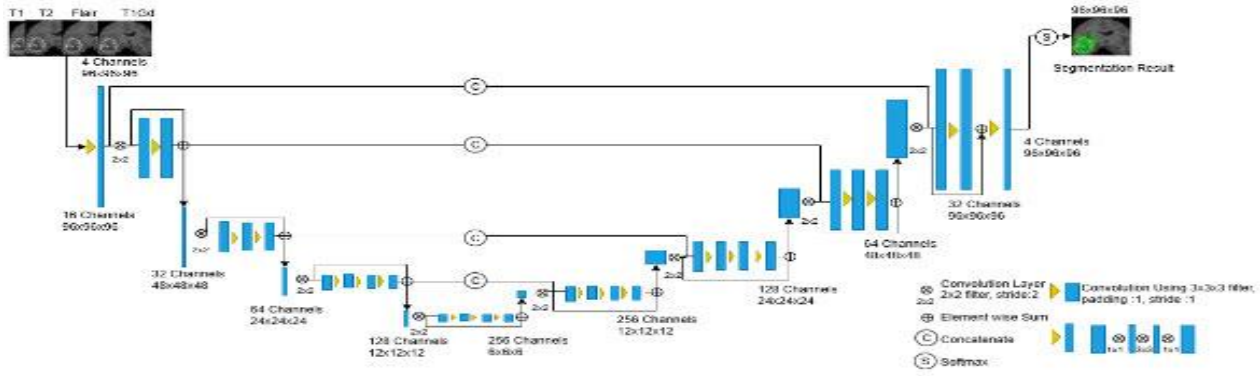

FIGURE 5. Architecture of V-Net.

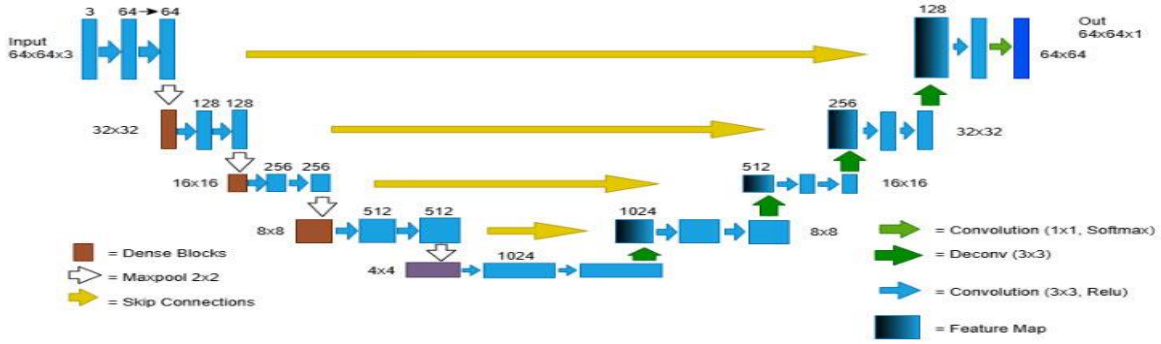

FIGURE 6. Architecture of DenseNet.

Fig. 13 indicates the performance of classifiers when missing data is recovered by NMTF. It can be seen that there is a reduction in the classification accuracies as the percentage of missing data increase from 10%–50%. However, DenseNet outperformed other classifiers for almost all cases of missing data. Fig. 13 further reports that the accuracies achieved by classifiers on NMTF recovered data are better as compared to NMF-recovered and CP-WOPT-recovered data, demonstrating the usefulness of the proposed framework.

B. PERFORMANCE OF PROPOSED STRATEGY ON DATASET 2

The performance of the proposed framework is assessed on Dataset 2 as well. Table 4 shows the performance of NMF, CP-WOPT and NMTF for different percentages of missing data. It is again evident that NMTF outperformed other methods as it achieved minimum RME even in the worst case, when 50% of the data was missing.

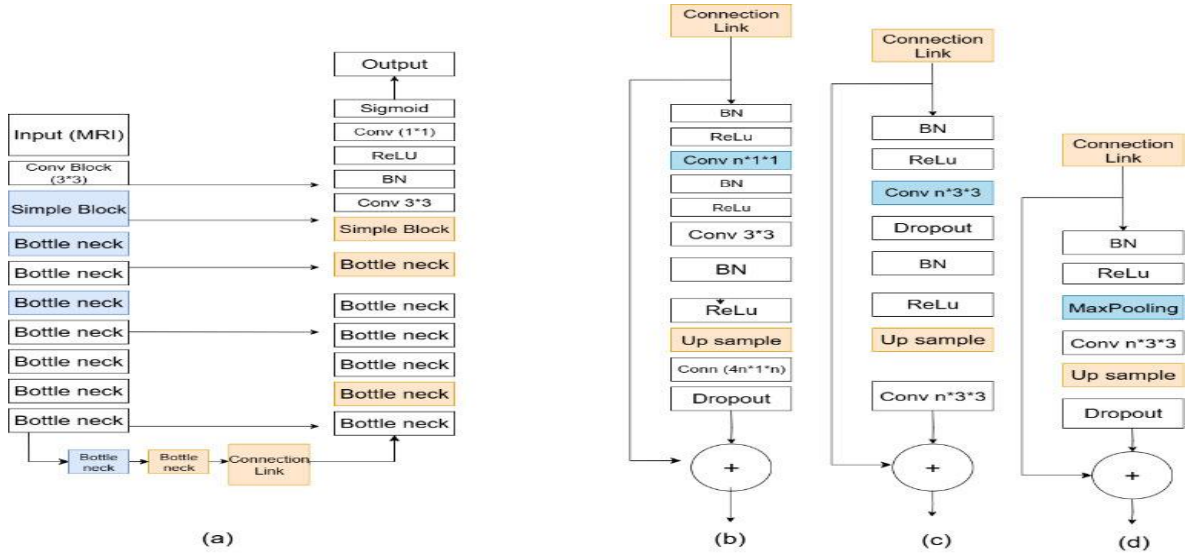

FIGURE 7. Architecture of ResNet: (a) Long skip connection process (b) Bottle neck process (c) Basic working (d) Simplified block.

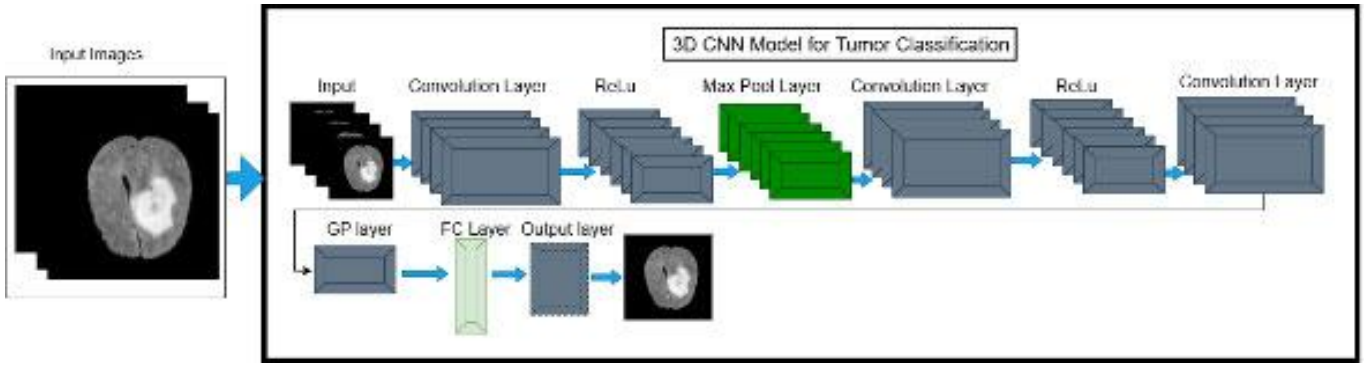

FIGURE 8. Architecture of CNN.

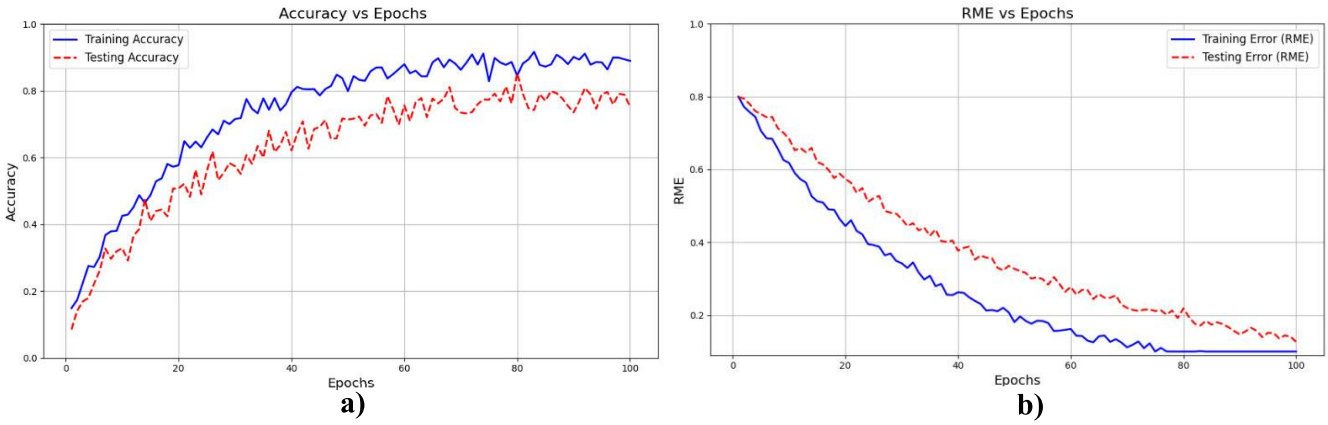

FIGURE 9. a) Accuracy vs Epochs graph b) RME vs Epochs graph; for dataset 1.

As reference accuracies are required for comparison, hence Table 5 presents the accuracies of six classifiers, when they are trained on data with no missing values (complete dataset). U-Net achieved the accuracy of up to 98%, outperforming all other methods. The results for classification with missing data are reported in Fig. 12. It must be noted that as percentage of missing data increase, accuracies deteriorate significantly. Fig. 14 shows the classification accuracy of various deep learning models for Dataset 2, when three imputation methods are employed to recover the missing data. The first section

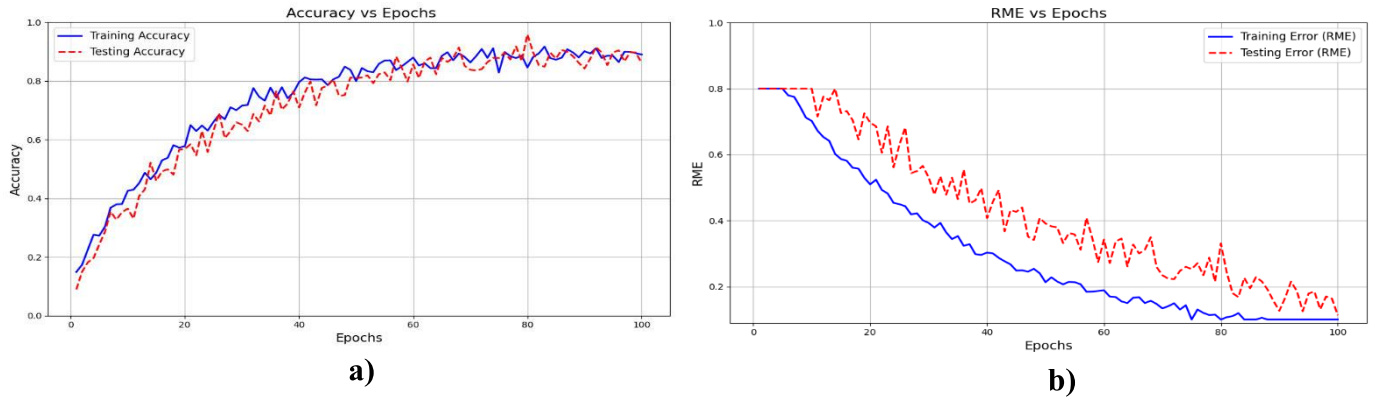

FIGURE 10. a) Accuracy vs Epochs graph b) RME vs Epochs graph; for dataset 2.

TABLE 2. Performance of imputation techniques on dataset 1.

Missing Data		10%	20%	30%	40%	50%
Imputation Methods	NMTF	0.21	0.26	0.34	0.39	0.41
	NMF	0.34	0.37	0.39	0.43	0.48
	CP-WOPT	0.25	0.29	0.36	0.43	0.45

TABLE 3. Accuracy of classifiers for dataset 1 without missing data.

Dataset 1		
Without missing data/ Complete Dataset	**Classifiers**	**Accuracy %**
	U-Net	92.8 ± 3.2%
	V-Net	92.2 ±2.1%
	DenseNet	96.2 ± 2.4%
	ResNet	85.3 ± 1.7%
	CNN	81.1 ± 2.4%
	FCN	75.5±1.31%

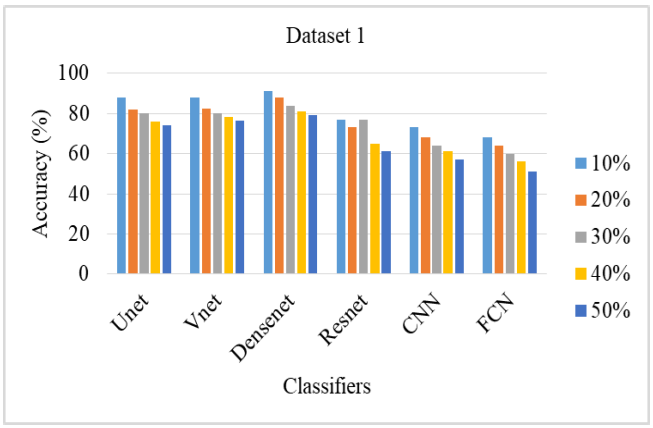

FIGURE 11. Performance of various classifiers on dataset 1 with 10% to 50% missing data.

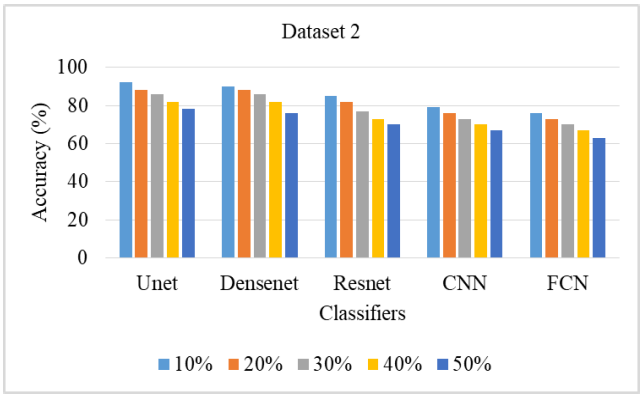

FIGURE 12. Performance of various classifiers on dataset 2 with 10% to 50% missing data.

(left-most part) of the Fig. 14 indicates the performance of classifiers when missing data is recovered by NMTF. It can be seen that there is a reduction in the classification accuracies as the percentage of missing data increase from 10%–50%. However, DenseNet outperformed other classifiers for almost all cases of missing data. Fig. 14 further reports that the accuracies achieved by classifiers on NMTF recovered data are better as compared to NMF-recovered and CP-WOPT-recovered data, demonstrating the usefulness of the proposed framework.

V. DISCUSSION

In this research, our primary inquiry revolved around the question of whether the recovery of missing data is important for classifiers as opposed to the conventional approach of neglecting the missing data leads to an improvement in problem-solving. To investigate this,

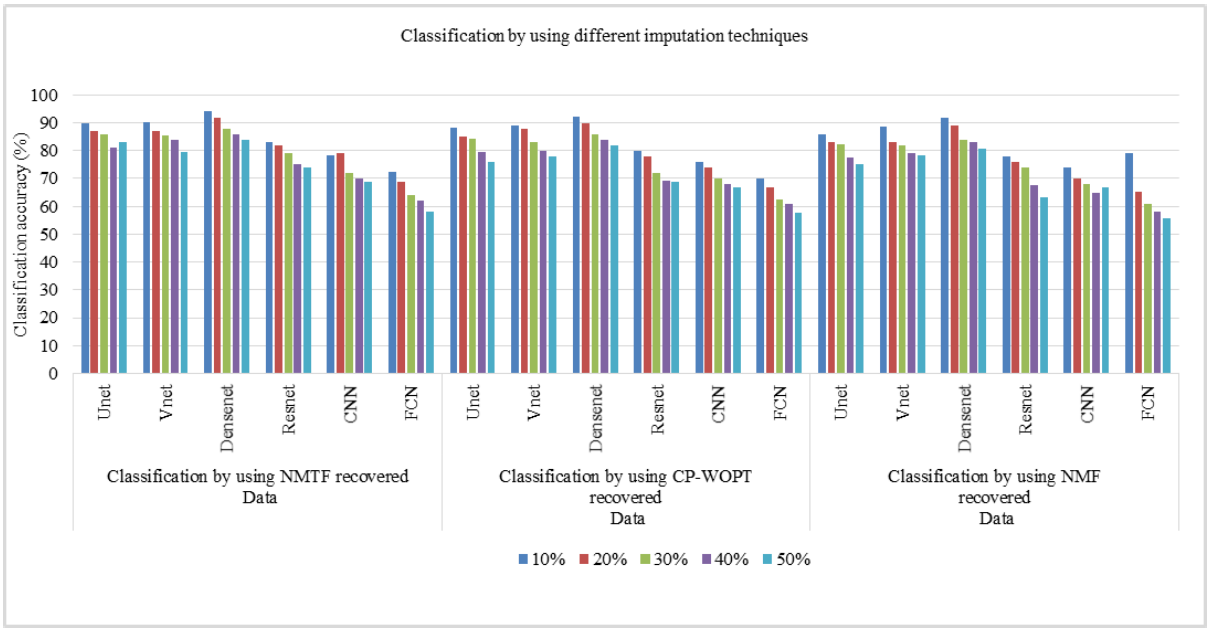

FIGURE 13. Performance of various classifiers on dataset 1 imputed by NMF, CP-WOPT and NMTF.

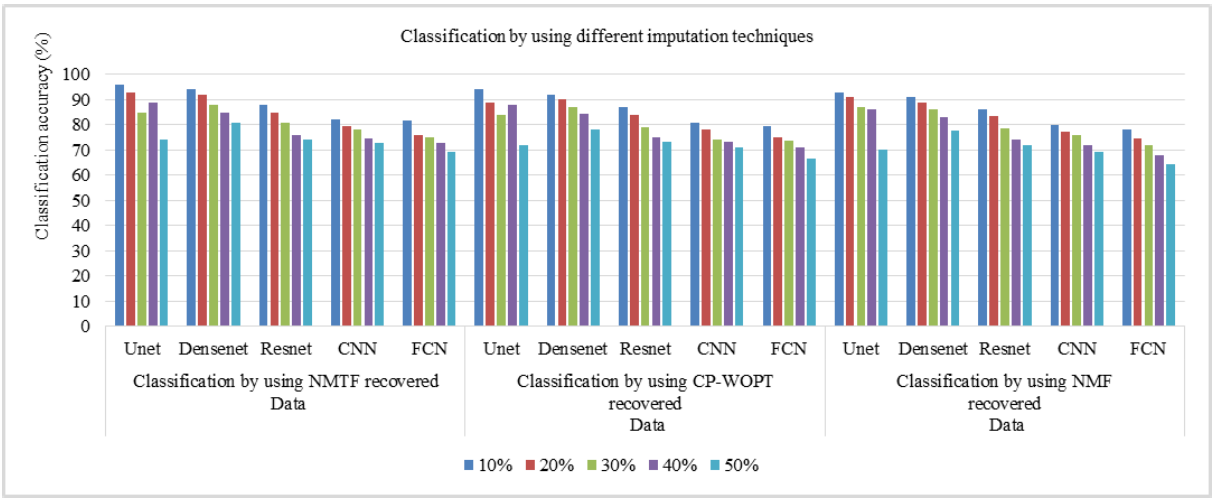

FIGURE 14. Performance of various classifiers on dataset 2 recovered by NMF, CP-WOPT and NMTF.

TABLE 4. Performance of imputation techniques on dataset 2.

Missing Data		10%	20%	30%	40%	50%
Imputation methods	NMTF	0.22	0.27	0.36	0.41	0.42
	NMF	0.35	0.38	0.41	0.44	0.5
	CP-WOPT	0.32	0.31	0.37	0.44	0.47

TABLE 5. Accuracy of classifiers for dataset 2 without missing data.

Dataset 2		
	Classifiers	Accuracy %
Without Missing Data/ Complete Dataset	U-Net	98 ± 2.1%
	V-Net	NA
	DenseNet	95.5 ± 1.5%
	ResNet	89 ± 3.3%
	CNN	83.5 ± 2.1%
	FCN	80 ± 3.4%

we employed tensor decomposition as one of the tools to delve into this matter. The ultimate findings on dataset I demonstrated a relative enhancement in performance accuracy of classifiers, validating our hypothesis.

For further validation, we applied the NMTF-based new approach to another dataset, and the same observation was noted in dataset II.

On the subject of diagnosing brain tumor, many studies have been performed so far, none of which used the concept of NMTF. According to the results obtained in this study, which are shown in Fig. 6 and Fig. 8, the use of this tensor decomposition method led to the increased accuracy of classification.

In this study, without using the tensor decomposition method, the average classification accuracy was 79.21%, which reached 88.6% using our proposed method in dataset I. To be further evaluate, our proposed method was tested on the second dataset, in which case the classification accuracy increased from 75.22% to 87.16% compared to the traditional method and therefore, our initial theory was proved.

The experiments show that ResNet performed better than other models for the dataset 1. The reason ResNet performs better is because residual connections help solve the vanishing gradient issue, and allow layers to become deeper which helps find and show more detailed tumor features in MRIs. The results showed that performance of U-Net almost matches ResNet due to the effective spatial information handling built into its encoder-decoder architecture.

The results further show that V-Net was able to handle volumetric image segmentation comparable to U-Net but is not as precise as ResNet. The three networks, DenseNet, FCN and CNN, performed slightly poor, suggesting they work better with other tasks rather than with brain tumor segmentation. FCN and CNN struggled because they do not have enough layers and do not capture hierarchy like the other models. The idea of tensor completion is especially important in clinics since weak images can lead to problems with automated assistance.

According to these results, MRI analysis powered by data completion and deep learning-based classification can assist clinicians in better planning treatments and improving how patients recover. More studies could concentrate on enhancing the versatility of the models Introduction using different datasets and trying architectures that blend the capabilities of several models.

A. LIMITATIONS AND FUTURE RECOMMENDATIONS

In this study, we employed several deep learning-based classifiers to complete, incomplete, and imputed MRI scans. However, encoder-decoder-based models tend to be over-parameterized and computationally intensive, especially in their 3D forms, making them susceptible to overfitting, particularly with limited medical datasets.

To address this, future work will focus on incorporating intelligent data augmentation strategies to expand the dataset and integrating attention mechanisms to enhance feature representation. Additionally, extending the research to include multi-modal data could further improve classification accuracy.

VI. CONCLUSION

The correct diagnosis of brain tumor can significantly reduce the progression of the disease to severe stages. However, due to the mild and ambiguous clinical symptoms, it is difficult and expensive to diagnose brain tumor. Moreover, data can miss in MRI scans because of various reasons such as hardware errors, voluntary motion and physiological motion of patients, metallic implants etc. In this study, it was found that classification accuracy of classifiers deteriorates as percentage of missing data increase. Therefore, rather than neglecting the missing data, we propose to first recover it by NMTF, and then use this NMTF-recovered data to train the classifiers. It was shown that classification significantly improves when classifiers are fed tensor-completed data rather than incomplete data. We evaluated the proposed framework on two datasets.

REFERENCES

[1] Z. Rasheed, Y.-K. Ma, I. Ullah, T. Al Shloul, A. B. Tufail, Y. Y. Ghadi, M. Z. Khan, and H. G. Mohamed, "Automated classification of brain tumors from magnetic resonance imaging using deep learning," *Brain Sci.*, vol. 13, no. 4, p. 602, Apr. 2023, doi: 10.3390/brainsci13040602.

[2] F. Ullah, M. Nadeem, M. Abrar, M. Al-Razgan, T. Alfakih, F. Amin, and A. Salam, "Brain tumor segmentation from MRI images using handcrafted convolutional neural network," *Diagnostics*, vol. 13, no. 16, p. 2650, Aug. 2023, doi: 10.3390/diagnostics13162650.

[3] X. Guan, G. Yang, J. Ye, W. Yang, X. Xu, W. Jiang, and X. Lai, "3D AGSE-VNet: An automatic brain tumor MRI data segmentation framework," *BMC Med. Imag.*, vol. 22, no. 1, p. 6, Dec. 2022, doi: 10.1186/s12880-021-00728-8.

[4] D. LaBella et al., "The ASNR-MICCAI brain tumor segmentation (BraTS) challenge 2023: Intracranial meningioma," 2023, *arXiv:2305.07642*.

[5] T. A. Soomro, L. Zheng, A. J. Afifi, A. Ali, S. Soomro, M. Yin, and J. Gao, "Image segmentation for MR brain tumor detection using machine learning: A review," *IEEE Rev. Biomed. Eng.*, vol. 16, pp. 70–90, 2023, doi: 10.1109/RBME.2022.3185292.

[6] A. R. M. Mehzooza, "Transformative applications of AI in biomedical imaging," *J. Inf. Syst. Eng. Manag.*, pp. 126–135, 2024, doi: 10.55267/iadt.2024.10455.

[7] S. Bakas, H. Akbari, A. Sotiras, M. Bilello, M. Rozycki, J. S. Kirby, J. B. Freymann, K. Farahani, and C. Davatzikos, "Advancing the cancer genome atlas glioma MRI collections with expert segmentation labels and radiomic features," *Sci. Data*, vol. 4, no. 1, Sep. 2017, Art. no. 170117, doi: 10.1038/sdata.2017.117.

[8] Z. Zhou, M. M. R. Siddiquee, N. Tajbakhsh, and J. Liang, "UNet++: Redesigning skip connections to exploit multiscale features in image segmentation," *IEEE Trans. Med. Imag.*, vol. 39, no. 6, pp. 1856–1867, Jun. 2020, doi: 10.1109/TMI.2019.2959609.

[9] F. Isensee, P. F. Jaeger, S. A. A. Kohl, J. Petersen, and K. H. Maier-Hein, "NnU-net: A self-configuring method for deep learning-based biomedical image segmentation," *Nature Methods*, vol. 18, no. 2, pp. 203–211, Feb. 2021, doi: 10.1038/s41592-020-01008-z.

[10] H. Mzoughi, I. Njeh, M. B. Slima, and A. Benhamida, "Glioblastomas brain tumor segmentation using optimized U-Net based on deep fully convolutional networks (D-FCNs)," in *Proc. 5th Int. Conf. Adv. Technol. Signal Image Process. (ATSIP)*, Sep. 2020, pp. 1–6, doi: 10.1109/ATSIP49331.2020.9231681.

[11] Y. Chen, "Automatic brain tumor segmentation using multi-task U-Net with graph propagation," *IEEE Trans. Med. Imag.*, vol. 42, no. 4, pp. 930–942, 2023.

[12] T. Mota, M. R. Verdelho, D. J. Araújo, A. Bissoto, C. Santiago, and C. Barata, "MMIST-ccRCC: A real world medical dataset for the development of multi-modal systems," in *Proc. IEEE/CVF Conf. Comput. Vis. Pattern Recognit. Workshops (CVPRW)*, Jun. 2024, pp. 2395–2403.

[13] R. Noor, A. Wahid, S. U. Bazai, A. Khan, M. Fang, U. A. Bhatti, and Y. Y. Ghadi, "DLGAN: Undersampled MRI reconstruction using deep learning based generative adversarial network," *Biomed. Signal Process. Control*, vol. 93, Jul. 2024, Art. no. 106218.

[14] X. Zhou, A. R. Balachandra, M. F. Romano, S. P. Chin, R. Au, and V. B. Kolachalama, "Adversarial learning for MRI reconstruction and classification of cognitively impaired individuals," *IEEE Access*, vol. 12, pp. 83169–83182, 2024.
[15] S. Ramadass, S. Narayanan, R. Kumar, and T. K, "Effectiveness of generative adversarial networks in denoising medical imaging (CT/MRI images)," *Multimedia Tools Appl.*, vol. 84, no. 20, pp. 21891–21915, Oct. 2024.
[16] B. A. Mohammed, E. M. Senan, T. H. Rassem, N. M. Makbol, A. A. Alanazi, Z. G. Al-Mekhlafi, T. S. Almurayziq, and F. A. Ghaleb, "Multi-method analysis of medical records and MRI images for early diagnosis of dementia and Alzheimer's disease based on deep learning and hybrid methods," *Electronics*, vol. 10, no. 22, p. 2860, Nov. 2021.
[17] G. Battineni, M. A. Hossain, N. Chintalapudi, E. Traini, V. R. Dhulipalla, M. Ramasamy, and F. Amenta, "Improved Alzheimer's disease detection by MRI using multimodal machine learning algorithms," *Diagnostics*, vol. 11, no. 11, p. 2103, Nov. 2021.
[18] L. Liu, S. Liu, L. Zhang, X. V. To, F. Nasrallah, and S. S. Chandra, "Cascaded multi-modal mixing transformers for Alzheimer's disease classification with incomplete data," *NeuroImage*, vol. 277, Aug. 2023, Art. no. 120267.
[19] C. Ding, T. Li, W. Peng, and H. Park, "Orthogonal nonnegative matrix T-factorizations for clustering," in *Proc. 12th ACM SIGKDD Int. Conf. Knowl. Discovery Data Mining*, Aug. 2006, doi: 10.1145/1150402.1150420.
[20] K. W. Wilson, B. Raj, P. Smaragdis, and A. Divakaran, "Speech denoising using nonnegative matrix factorization with priors," presented at the *Proc. IEEE Int. Conf. Acoust., Speech Signal Process.*, Las Vegas, NV, USA, Mar. 2008, doi: 10.1109/ICASSP.2008.4518538.
[21] A. Cichocki, "Non-negative matrix factorization with α-divergence," vol. 29, no. 9, pp. 1433–1440, Mar. 2008.
[22] D. L. Sun and C. Févotte, "Alternating direction method of multipliers for non-negative matrix factorization with the beta-divergence," presented at the *Proc. IEEE Int. Conf. Acoust., Speech Signal Process. (ICASSP)*, Florence, Italy, May 2014, doi: 10.1109/ICASSP.2014.6854796.
[23] S.-J. Kim, T. Hwang, and G. B. Giannakis, "Sparse robust matrix trifactorization with application to cancer genomics," presented at the *Proc. 3rd Int. Workshop Cognit. Inf. Process. (CIP)*, Baiona, Spain, May 2012, doi: 10.1109/CIP.2012.6232906.
[24] H. Kim and H. Park, "Nonnegative matrix factorization based on alternating nonnegativity constrained least squares and active set method," *SIAM J. Matrix Anal. Appl.*, vol. 30, no. 2, pp. 713–730, Jan. 2018, doi: 10.1137/07069239x.
[25] A. Cichocki and A. Shun-Ichi, *Nonnegative Matrix and Tensor Factorizations: Applications to Exploratory Multi-Way Data Analysis and Blind Source Separation*, Sep. 2009, doi: 10.1002/9780470747278.
[26] (2020). *Brain Tumor Segmentation 2020 Dataset*. [Online]. Available: https://www.kaggle.com/awsaf49/brats20-dataset-training-validation
[27] [Online]. Available: https://www.kaggle.com/datasets/pkdarabi/brain-tumor-image-dataset-semantic-segmentation
[28] S. A. Qureshi, L. Hussain, U. Ibrar, E. Alabdulkreem, M. K. Nour, M. S. Alqahtani, F. M. Nafie, A. Mohamed, G. P. Mohammed, and T. Q. Duong, "Radiogenomic classification for MGMT promoter methylation status using multi-omics fused feature space for least invasive diagnosis through mpMRI scans," *Sci. Rep.*, vol. 13, no. 1, p. 3291, Feb. 2023.
[29] Q.-U.-A. Chaudhary, S. A. Qureshi, T. Sadiq, A. Usman, A. Khawar, S. T. H. Shah, and A. U. Rehman, "SAlexNet: Superimposed AlexNet using residual attention mechanism for accurate and efficient automatic primary brain tumor detection and classification," *Results Eng.*, vol. 25, Mar. 2025, Art. no. 104025.

WAQAS MEHMOOD (Member, IEEE) was born in Sargodha, Pakistan. He received the B.S. degree in electronics technology from the University of Lahore, Pakistan, in 2014, and the M.S. degree in engineering management and the M.S. degree in biomedical engineering from Superior University, Pakistan, in 2017 and 2024, respectively. Since 2014, he has been with Shaukat Khanum Memorial Cancer Hospital, Lahore, Pakistan, where he is currently a Senior Biomedical Engineer, with specialized focus on radiological equipment. He holds NSF Enhanced Biosafety Cabinet Certification and Sterile Compounding Facility (CETA) Certification from the USA.

AQSA SAJJAD received the bachelor's degree in biomedical engineering from the University of Engineering and Technology (UET), Lahore, Pakistan, in 2022, and the master's degree in biomedical engineering from Riphah International University, Pakistan, in 2024. During her undergraduate studies, she contributed to the development of a prosthetic arm, culminating in a conference paper published with IEEE, in 2022. Her final year project on the prosthetic arm was funded by Ignite. Since 2023, she has been a Biomedical Engineer with the Shaukat Khanum Memorial Cancer Hospital and Research Center, Lahore. She is a registered engineer with Pakistan Engineering Council (PEC).

MUHAMMAD AKMAL received the M.S. degree in electrical engineering from the National University of Sciences and Technology, Islamabad, Pakistan, in 2014, and the Ph.D. degree in electronic engineering from International Islamic University, Islamabad, in 2020. From 2022 to 2024, he was an Assistant Professor with Riphah International University, Lahore, Pakistan. Since 2025, he has been an Assistant Professor with the Electrical Engineering Department, National University of Computer and Emerging Sciences, Lahore. He is the author of many articles in reputed journals and conferences. His research interests include biomedical signal and image processing, machine learning, and deep learning.

FATIMA KAINAT received the Bachelor of Medicine and Bachelor of Surgery (M.B.B.S) degree from Sahiwal Medical College, Sahiwal, Pakistan, in 2016. She has one-year house job experience with Sahiwal Medical College, until May 2018. From 2019 to 2021, she was with the Women Medical Officer with the Radiology Department, Wazir Hospital, Lahore. She was with the Women Medical Officer with the Department of Pediatric Oncology, Shaukat Khanum Memorial Cancer Hospital and Research Centre, Pakistan, in 2022. She is currently in the latter phase of her four-year training of FCPS Diagnostic Radiology Residency Program with the CMA Teaching Hospital, Pakistan.